Comparing visual cortex of children and adults reveals a late-stage change in the architecture of V1

Marc M. Himmelberg[1,2,*], Ekin Tünçok[1], Jesse Gomez[3], Kalanit Grill-Spector[4,5], Marisa Carrasco[1,2,^] & Jonathan Winawer[1,2,^]

AFFILIATIONS:
[1] Department of Psychology, New York University, New York, NY, 10003, USA
[2] Center for Neural Science, New York University, New York, NY, 10003, USA
[3] Princeton Neuroscience Institute, Princeton University, Princeton, NJ, 08540, USA
[4] Department of Psychology, Stanford University, Stanford, CA, 94305, USA
[5] Wu Tsai Neurosciences Institute, Stanford University, Stanford, CA, 94305, USA
[^] Equal contributors
* Corresponding author: Marc M. Himmelberg (marc.himmelberg@nyu.edu)

KEYWORDS: retinotopy, visual development, cortical magnification, early visual cortex, fMRI

ABSTRACT

Adult visual ability differs markedly with stimulus polar angle: relative to the point of fixation, visual performance is best for stimuli to the left or right, intermediate for stimuli below, and poorest for stimuli above. These polar angle asymmetries in performance are paralleled by cortical asymmetries in the visual field representation in primary visual cortex (V1). Whereas children, like adults, show better performance for stimuli along the horizontal than the vertical meridian, they show no performance difference for stimuli above vs below fixation. Is the difference in visual performance between children and adults matched by a difference in the amount of V1 surface area representing these regions? We used fMRI to measure the distribution of the cortical surface representing the visual field in children and adults. Two properties of the V1, V2, and V3 maps were mature in children –overall map surface area and variation in surface area as a function of eccentricity. Further, like adults, children had much greater V1 surface area representing the horizontal than vertical meridian. However, unlike adults, children did not have greater V1 surface area for the lower than upper vertical meridian. These data indicate a late-stage change in the architecture of V1 that may drive the emergence of a visual performance asymmetry along the vertical meridian by adulthood.

INTRODUCTION

A central question in systems neuroscience is whether and how the organization of cortical maps changes across the lifespan. Some properties of human early visual cortex mature early; functional MRI studies show that visual field map surface area (Dekker et al., 2019), population receptive field (pRF) sizes (Dekker et al., 2019; Gomez et al., 2018), and the change in cortical magnification with eccentricity (Conner et al., 2004; Dekker et al., 2019) are adult-like by childhood (6-12 years). In contrast, performance on some basic visual tasks such as vernier acuity (Skoczenski and Norcia, 2002), contour integration (Kovács, 2000; Kovács et al., 1999), and texture segmentation (Sireteanu, 2000) do not mature until adolescence (13+ years) (Braddick and Atkinson, 2011). Whereas many properties of primary sensory cortices, including V1, mature early in development (Bourne and Rosa, 2006; Flechsig, 1920; Lebenberg et al., 2019), these behavioral findings suggest that V1 likely develops across a longer period than shown by fMRI studies.

One striking difference in visual performance between adults and children pertains to polar angle asymmetries. Both adults and children show better visual performance for stimuli along the horizontal than vertical meridian at a matched eccentricity (horizontal-vertical asymmetry; HVA) (Carrasco et al., 2022). However, only adults show better visual performance for stimuli along the lower than upper vertical meridian (vertical meridian anisotropy; VMA) for a variety of perceptual tasks (e.g., orientation, contrast sensitivity, acuity; (Abrams et al., 2012; Barbot et al., 2021; Carrasco et al., 2001; Greenwood et al., 2017; Himmelberg et al., 2020). Instead, children's visual performance is similar between the upper and lower vertical meridian (Carrasco et al., 2022).

In adults, the polar angle asymmetries in visual performance are well matched to cortical magnification; there is more V1 tissue representing the horizontal than vertical meridian, and the lower than upper vertical meridian of the visual field (Benson et al., 2021a; Himmelberg et al., 2021, 2022a; Silva et al., 2018). These cortical polar angle asymmetries have not been quantified in children. Because visual performance asymmetries along the vertical meridian differ between children and adults, we hypothesize that the cortical asymmetry along the vertical meridian representation in V1 may also differ between children and adults.

Here, we quantified and compared the distribution of cortical surface area representing the visual field between adults and children. We used fMRI-based population receptive field (pRF) modeling to measure retinotopic maps in early visual cortex (V1, V2, and V3) in 24 adults (22-26 years old) and 24 children (5-12 years old). We compared the following metrics of the cortical representation of the visual field:

1. The surface area of the V1, V2, and V3 maps
2. Areal cortical magnification as a function of eccentricity within each of V1, V2, and V3
3. Cortical surface area as a function of polar angle in V1, comparing the representation of the horizontal and vertical meridians, and the lower and upper vertical meridians of the visual field.

Based on prior work, we hypothesized that the first two measures would be similar between adults and children, whereas the third might differ given the different pattern of visual performance along the vertical meridian between adults and children.

Indeed, we found that within V1, V2 and V3, total surface area and cortical magnification as a function of eccentricity were similar between adults and children. We also found that both adults and children had much more V1 surface area representing the horizontal than vertical meridian of the visual field, consistent with better visual performance along the horizontal than vertical meridian in both groups (Abrams et al., 2012; Barbot et al., 2021; Carrasco et al., 2001, 2022; Greenwood et al., 2017; Himmelberg et al., 2020). However, whereas adults had more V1 surface area representing the lower than the upper vertical meridian (again, in agreement with prior measures), children did not, consistent with children's visual performance at these locations. This difference in the cortical representation of the vertical meridian between adults and children reveals a surprisingly large late-stage change in cortical architecture of V1 and parallels the emergence of a vertical meridian asymmetry in visual performance.

RESULTS

High quality retinotopic maps measured in adults and children

First, a series of quality checks were run on the retinotopy data to determine whether the maps were comparable between adults and children. We quantified the amount of variance the pRF models explained in the BOLD time series in V1, V2, and V3. We also quantified the left-right hemisphere symmetry of the maps in individual participants.

In adults and children, visual inspection of the retinotopic maps indicated clear polar angle and eccentricity representations that were organized as expected for V1, V2, and V3. Examples of polar angle and eccentricity maps for two adults and two children are illustrated in **Fig. 1A and B** and additional maps on inflated surfaces are available in prior work using the same dataset (Gomez et al., 2018). To complement the subjective assessment of the maps, for each participant, we computed the median variance explained (R^2) of the BOLD time series by the pRF fits for vertices within V1, V2, and V3 **(Fig. 1C)**. The R^2 of the pRF fits was high for both adults and children, indicating high quality data. Across V1, V2, and V3, the group median R^2 was between 0.60 and 0.80 (vertical dashed lines in **Fig. 1C**). Within each map, for adults and children respectively, the group median R^2 ranged between: 0.76 – 0.66 for V1, 0.71 – 0.64 for V2, and 0.72 – 0.70 for V3. A supplementary analysis showed that although there was more within-scan

motion for children than adults, motion was not correlated with the R^2 of the pRF fits in V1, V2 and V3 for either group (**Supplementary Fig. S1**), indicating that the quality of the retinotopic maps was robust against within-scan motion.

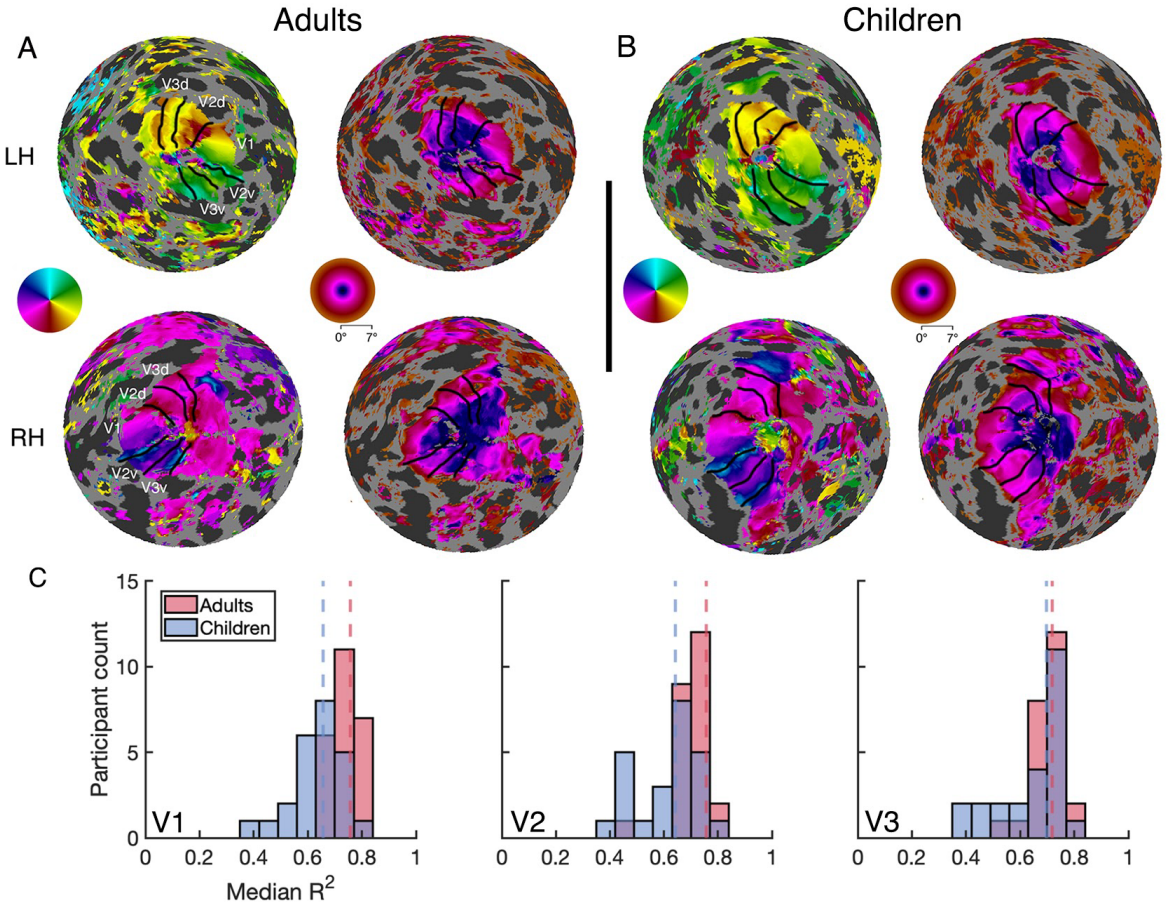

Fig 1. Example retinotopic maps and the variance explained of early visual field maps. Examples of polar angle and eccentricity maps (0-7°) from **(A)** two adults and **(B)** two children. Each hemisphere comes from a unique participant. The maps are presented on cortical flatmaps of the *fsnative* surface with the occipital pole in the center of the map. V1, V2, and V3 boundaries are indicated as black lines. **(C)** Histograms of the median variance explained (R^2) of V1, V2, and V3 for adults (in red) and children (in blue). Dashed red and blue lines reflect the group-level median R^2 for adults and children, respectively.

Prior work has shown that the left and right hemispheres of visual maps are similar in size (Benson et al., 2021b; Dougherty et al., 2003). Thus, an additional metric of data quality is the correlation of the surface area of the left and right hemispheres of the maps. This metric depends on the entire processing pipeline, from data acquisition, to pRF model fitting, to manual delineation of the ROIs, as noise at any stage of the pipeline could lower the correlation between hemispheres. For adults and children, the surface area of the left and right hemispheres of V1, V2, and V3 were all highly correlated **(Fig. 2)**. The high level of symmetry, and the similar correlation coefficients for adults and children, indicate that the maps are of similarly good quality.

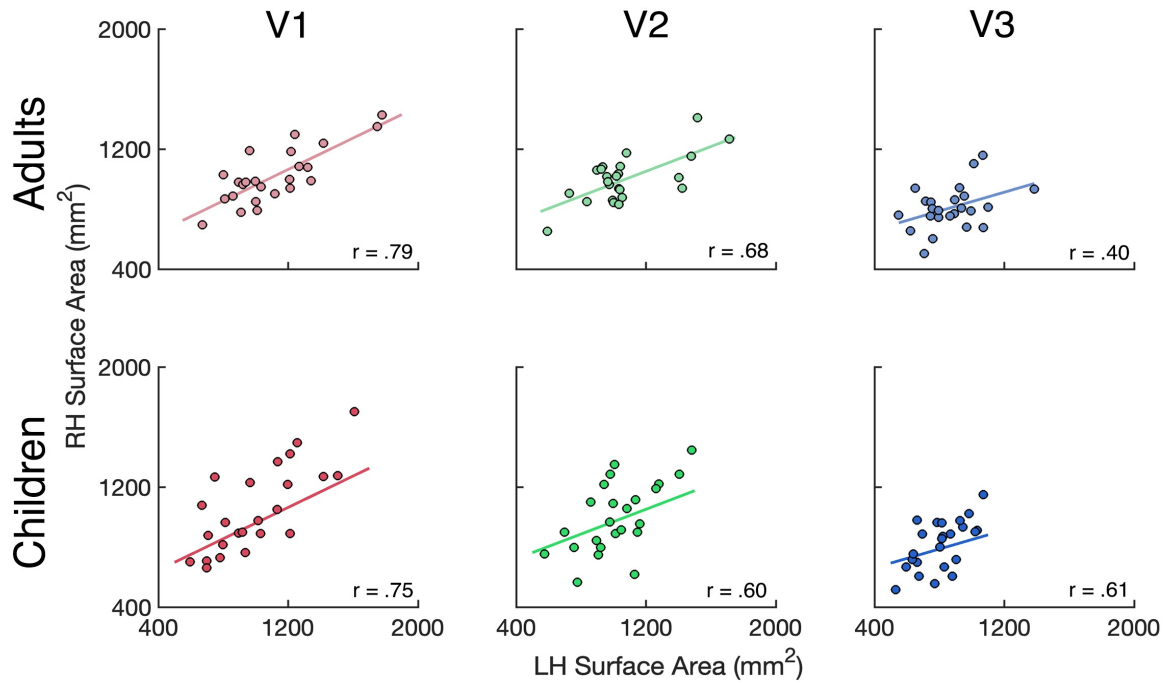

Fig 2. Correlations of the surface area between left and right hemispheres of early visual field maps. The colored line represents a line of best fit through the data showing the positive correlation between the left and right hemispheres of each ROI for adults (n=24) and children (n=24). All Pearson's correlations $p < 0.01$ except adult V3, where $p < 0.05$.

The surface area of early visual field maps is similar for adults and children

Next, we quantified the overall surface area (mm^2) of the V1, V2, and V3 maps within the 0-7° eccentricity range defined by our stimulus extent. The central 7° is 38% of the entire V1 map, according to the formula for areal cortical magnification proposed by Horton and Hoyt (1991). The surface areas were summed across the left and right hemisphere of each map within an individual participant.

First, we compared the mean surface area of the visual field maps for adults and children. Unpaired t-tests found that the surface area of V1, V2, and V3 did not significantly differ between adults and children (all $p > 0.1$). For each of V1, V2, and V3, the central tendency was highly similar between the two groups, whether measured as median (**Fig. 3A**) or mean (**Table 1**). Specifically, map surface area for adults was only slightly larger than for children (median: 1.5-2% and mean: 2-4% larger across V1-V3). For both adults and children, V2 was similar in size to V1, and V3 was smaller than V1 and V2. Further, because the total surface area of the cortex was similar between adults and children (1.8% larger for adults, $p = 0.169$) (**Fig. 3B**), the means remained similar between groups after normalizing the surface area of each participant's visual map by the total surface area of their cortex (all $p > 0.5$). We assessed sex differences in the surface area of the maps and found no difference in the surface area of V1, V2, or V3 when comparing between male and female adults (all $p > 0.1$), male and female children (all $p > 0.5$),

or when the surface area of each individual's map was normalized to the total surface area of their cortex (all $p > 0.1$).

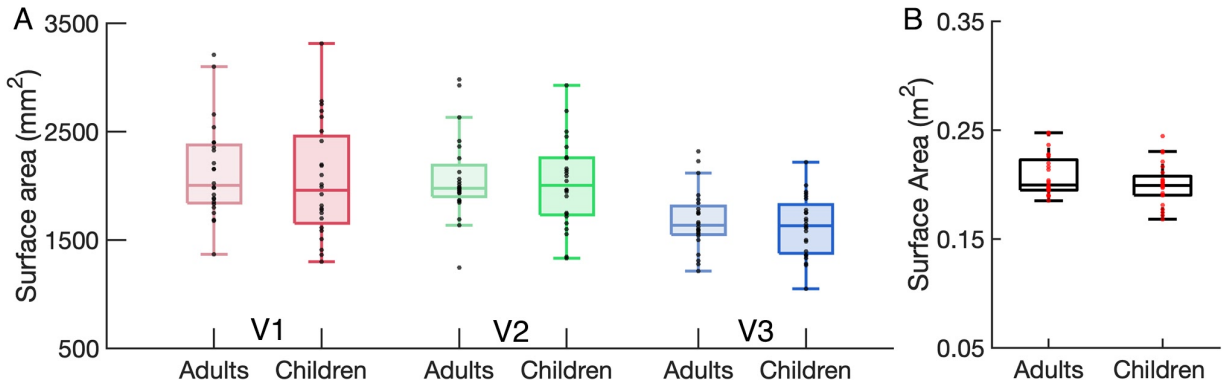

Fig 3. Measurements of the surface area of early visual field maps and the cortical sheet. (A) Surface area (mm^2) of V1, V2, and V3 for adults (n=24) and children (n=24). Individual data are plotted as black data points and the colored horizontal line represents the group-median surface area. Because the surface areas are summed across hemispheres, the values are about double those in Fig. 2. **(B)** The total surface area of the cortical sheet for adults and children. Individual data are plotted as red data points and the black horizontal line represents the median surface area. For both **(A)** and **(B)**, the top and bottom edges of each box represent the 75th and 25th percentiles, respectively, and the whiskers extend to the maxima and minima data points not considered outliers. The y-axes are matched so that the scaling in **(B)** is 100x the size of that in **(A)**.

We then compared the variability in map surface area in the two groups. We calculated the coefficient of variation (σ / μ) for each of the three maps across participants (**Table 1**). Variability in the surface area of the maps was similar for adults and children. Notably, the surface area of adult V1 varied more than twofold, consistent with prior measurements (Benson et al., 2021b; Dougherty et al., 2003; Himmelberg et al., 2022a); the smallest V1 was 1367 mm^2 and the largest was 3206 mm^2. The same variability in V1 surface area was found in children; the smallest V1 was 1297 mm^2 and the largest was 3312 mm^2. The coefficient of variation was also similar for the groups in V2 and V3.

	V1		**V2**		**V3**	
	Mean	**CV**	**Mean**	**CV**	**Mean**	**CV**
Adults	2129 mm^2	0.21	2067 mm^2	0.19	1680 mm^2	0.16
Children	2045 mm^2	0.26	2018 mm^2	0.20	1623 mm^2	0.17

Table 1. Mean surface area and coefficient of variation (CV) for early visual field maps. The mean surface area is calculated as the combined left and right hemispheres of the map defined from 0-7° eccentricity. The CV reflects the variability of surface area of a field map relative to its mean and is calculated as the standard deviation of surface area / mean surface area.

Within-scan motion presents the largest source of noise during fMRI (Friston et al., 1996) and children tend to move more than adults in the scanner (Fassbender et al., 2017; Poldrack et al.,

2002), To assess whether differences in within-scan motion impact surface area measurements, we correlated the surface area of each participant's ROI with their within-scan motion. ROI surface area and participant motion did not correlate for adults or children ($p > 0.1$). This is because early visual field maps are defined by explicit polar angle and eccentricity boundaries, not by a signal-to-noise ratio threshold.

Cortical magnification as a function of eccentricity in early visual field maps is similar between adults and children.

The amount of cortical surface area dedicated to processing the visual field decreases with increasing eccentricity from the center of visual space (Holmes and Lister, 1916; Inouye, 1909) and is called cortical magnification (Daniel and Whitteridge, 1961). We calculated areal cortical magnification (mm^2 of surface area/deg^2 of visual space) as a function of eccentricity (between 1° and 7°) for V1, V2, and V3. Areal cortical magnification was calculated by summing the surface area of vertices that fell within an eccentricity ring. The summed surface area was then divided by the area of visual space encapsulated by the eccentricity ring. This eccentricity ring was stepped across the cortical surface, from 1° to 7° of eccentricity. The ring began at 1° eccentricity rather than 0º because noise in the pRF estimates of retinotopic coordinates near the foveal confluence tends to be large (Dougherty et al., 2003; Himmelberg et al., 2021; Schira et al., 2009) and because the fixation task covered the central 0.5° of the display during the pRF mapping procedure. As the cortical magnification calculation is a fraction –with degree of visual space in the denominator– noisy estimates of small values will have a large effect on the computed fraction.

In V1, V2 and V3, cortical magnification decreased as a function of eccentricity, as expected **(Fig. 4)**. In V1, for eccentricities above 1.5°, the cortical magnification function of eccentricity in both adults and children was close to the estimates derived from the adult lesion data from Horton and Hoyt (1991). The estimates below 1.5º are noisier for the reasons described above. Overall, the cortical magnification function was highly similar between adults and children in all three maps. There is a hint of one subtle difference between groups in V2 and V3: in these maps, especially V2, adults had slightly more surface area representing central parts of the visual field than children. We return to this point in the Discussion.

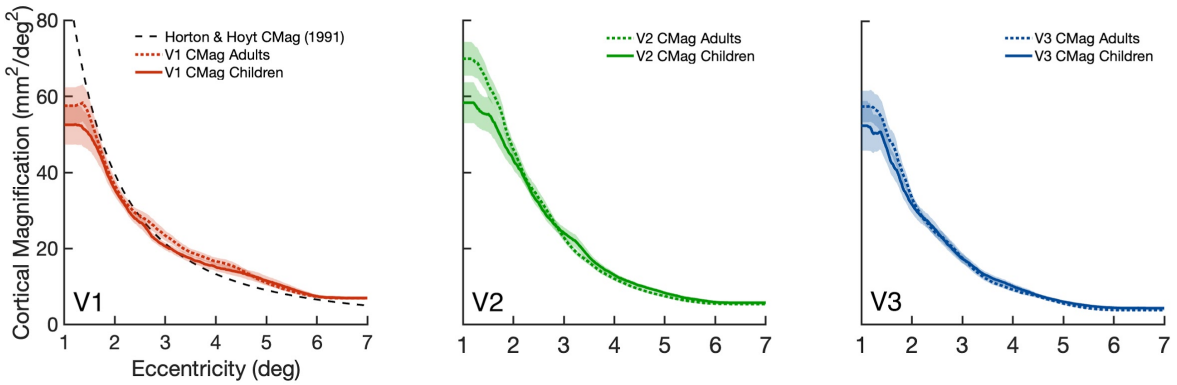

Fig. 4. Group-level areal cortical magnification as a function of eccentricity. Adults (n=24) are plotted as the dotted colored line and children (n=24) are plotted in the solid colored line. The black dashed line in panel (A) represents the cortical magnification function of V1 reported by Horton and Hoyt (1991). Shaded error bars are ±1 standard error of the mean (SEM).

Polar angle asymmetries in V1 surface area differ between adults and children

Next, we examined polar angle asymmetries in V1 surface area. We focused on V1 rather than V2 and V3 because V1 is a large, continuous map of the contralateral hemifield whereas V2 and V3 are both split into quarterfields, making it more difficult to robustly assess surface area as a function of fine changes in polar angle (though see (Silva et al., 2018) for measures of V2/V3 in adults). Recent studies have identified polar angle asymmetries in V1 surface area in adults; there is more V1 surface area (thus cortical tissue) representing the horizontal than vertical meridian, and the lower than upper vertical meridian of the visual field (Benson et al., 2021a; Himmelberg et al., 2021, 2022a; Silva et al., 2018). Here, we quantified these cortical polar angle asymmetries in children. For each participant, we calculated the V1 surface area representing angular wedge-ROIs that were centered on the left and right horizontal, upper vertical, and lower vertical meridians of the visual field. The wedge-ROIs gradually increased in width, from ±10° to ±50°, and spanned 1-7° of eccentricity. This eccentricity range was chosen to exclude the central 1° which can include noisy polar angle position estimates.

First, we examined the adult data and confirmed a cortical horizontal-vertical anisotropy (HVA) and vertical-meridian asymmetry (VMA). Specifically, there was more V1 surface representing the horizontal than vertical meridian (**Fig. 5A**), and the lower than upper vertical meridian (**Fig. 5B**). These polar angle asymmetries were large and were consistent with increasing wedge size up to ±50°. These measurements were made on the midgray surface. Given that surface area calculations depend on the cortical depth used to derive the surface area of each vertex, we also conducted these analyses on the pial and white matter surfaces and similarly identified a cortical HVA and VMA (**Supplementary Fig. S2A and B, and Fig. S3A and B**).

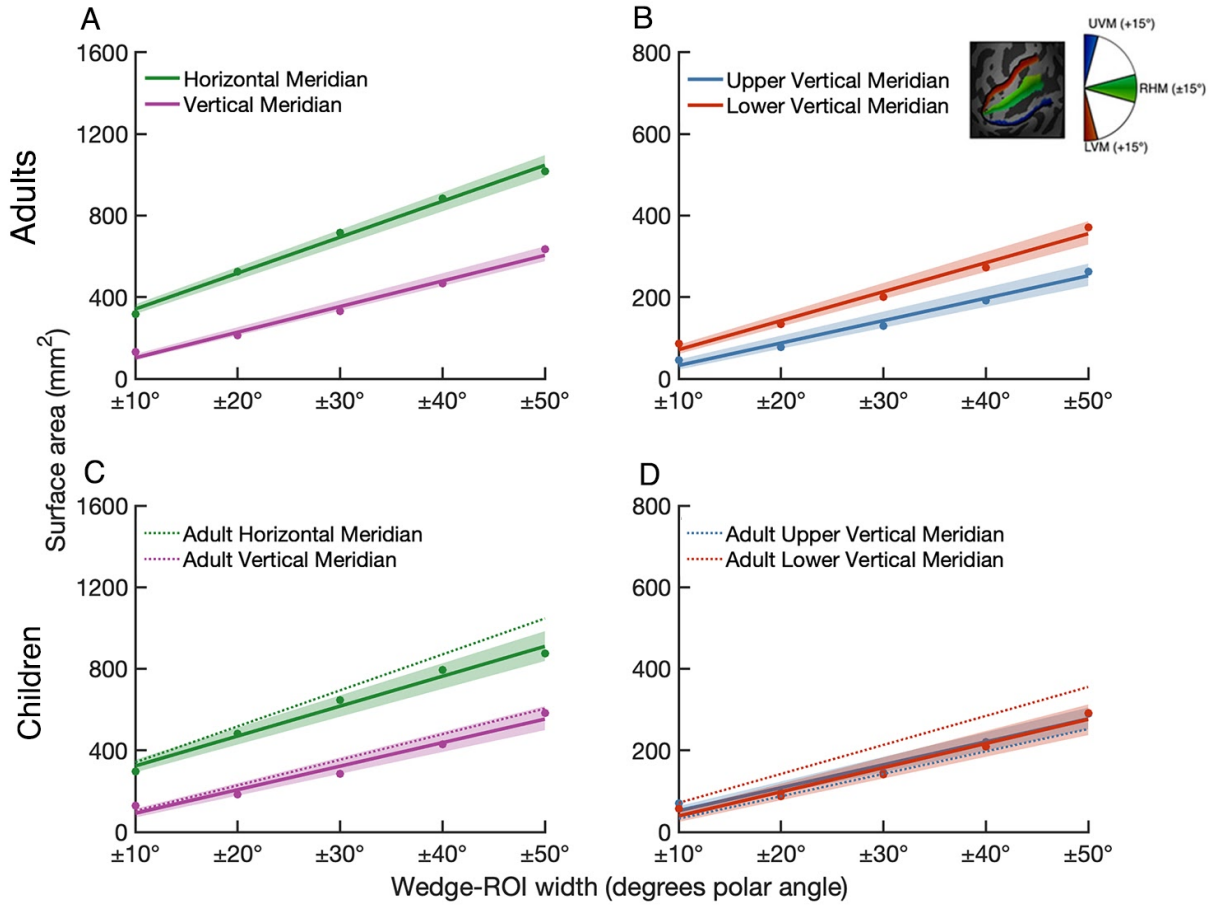

Fig. 5. Polar angle asymmetries in V1 surface area for adults and children. (A and C) V1 surface area (mm^2) measurements for wedges centered on the horizontal and vertical meridians, plotted as a function of wedge-width for adults (n=24) and children (n=24). **(B and D)** V1 surface area measurements for wedges centered on the upper and lower vertical meridians, plotted as a function of wedge-width, for adults and children. Colored lines represent the average of 10,000 bootstrapped linear fits to the data. The colored data points represent the bootstrapped mean at each wedge-ROI width. The shaded error bar represents the 68% bootstrapped confidence interval of a linear fit to the data. The dotted lines in **(C)** and **(D)** are the adult surface area measurements replotted for comparison to children.

We then quantified V1 surface area as a function of polar angle in children. We identified a cortical HVA in children; there was more V1 surface representing the horizontal than vertical meridian **(Fig. 5C)**. The effect was robust and similar to that observed in adults. However, unlike adults, children did not show greater surface areas for the lower than upper vertical meridian (**Fig. 5D**). Repeating these analyses on the pial and white matter surfaces similarly identified a cortical HVA but no VMA (**Supplementary Fig. S2C and D, and Fig. S3C and D**).

Children have less surface area representing the lower vertical meridian than adults

These data show that there is a striking difference between adults' and children's cortical representation of the vertical meridian. Unlike adults, children had no cortical VMA; there was no difference in the amount of V1 surface area representing the lower and upper vertical meridian.

The data in **Fig. 5D** show a pattern of children having less surface area representing the lower vertical meridian than adults, whereas the amount of surface area representing the upper vertical meridian is similar between the two groups.

The difference in the vertical meridian representation between adults and children was evident in the retinotopic maps of individual participants. In **Fig. 6** we visualize polar angle maps on inflated native cortical surfaces, angled to present the dorsal and ventral boundaries of V1 that represent the lower and upper vertical meridians (see legend inset). Inspection of the maps showed that adults have a thick red stripe along the dorsal V1/V2 border, representing the surface area of the lower vertical meridian. Conversely, children show a much thinner red stripe, indicating a constricted representation of the lower vertical meridian that encompasses less cortical surface area.

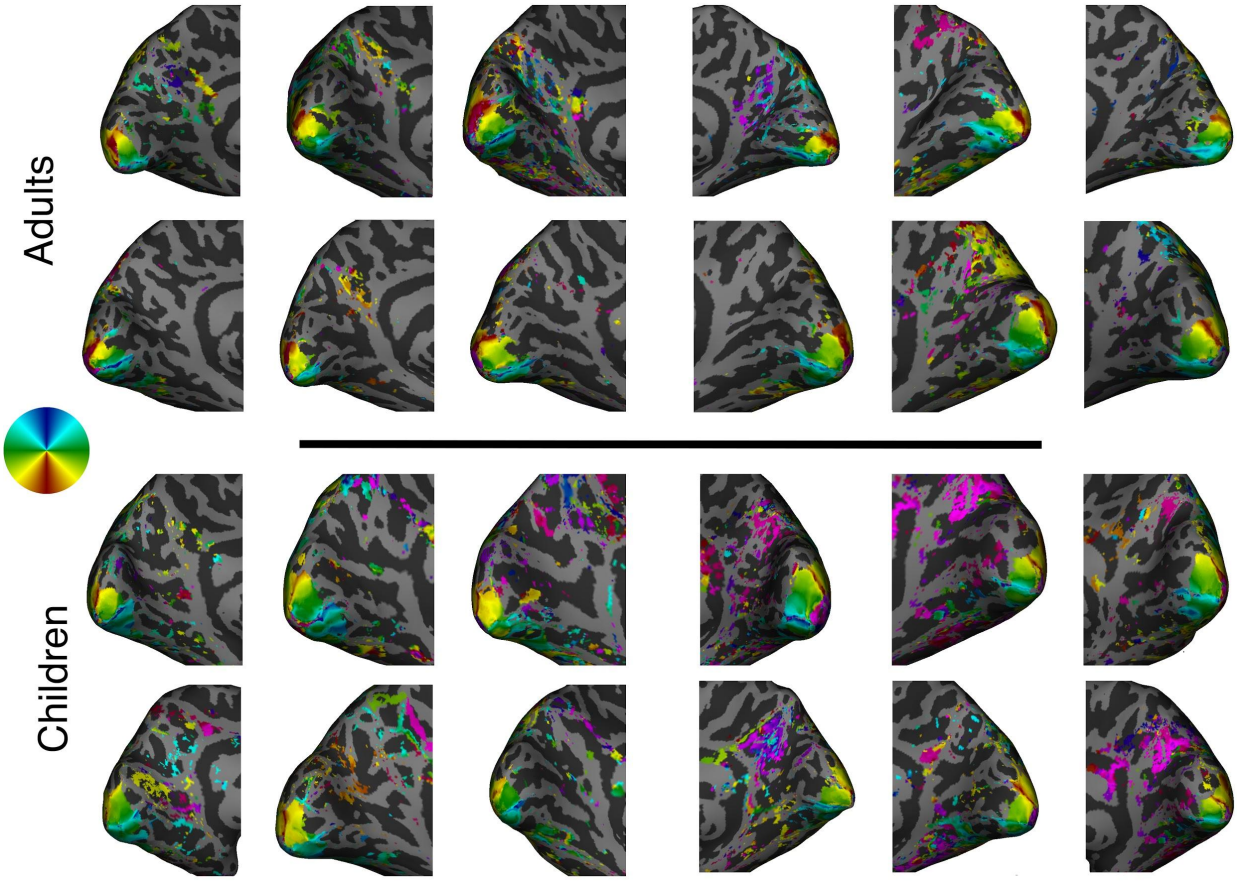

Fig 6. Polar angle maps for adults and children. Polar angle maps projected onto the left and right hemispheres of the inflated native surfaces are angled to present V1. Each hemisphere is from a unique participant. Red polar angle data represents the lower vertical meridian, blue data represents the upper vertical meridian, and green data represents the horizontal meridian (see polar angle legend inset). Children had a thinner lower vertical meridian representation (red data) than adults, congruent with a reduced cortical representation of the lower vertical meridian of the visual field.

Next, we parameterized the cortical asymmetries to describe the magnitude of the cortical HVA and VMA. Here, we used the V1 surface area measurements taken from the ±10° wedge-ROIs, thus the surface area measurements closest to each of the four polar angle meridians. First, for each participant, we calculated an asymmetry index for the HVA as:

$$Cortical\ HVA = \frac{(horizontal\ surface\ area - vertical\ surface\ area)}{mean(horizontal\ surface\ area, vertical\ surface\ area)} \times 100 \qquad (1)$$

A cortical HVA index of 0 indicates no difference in surface area between the horizontal and vertical meridian. As the asymmetry between the horizontal and vertical meridians increases, so does the magnitude of the cortical HVA.

Likewise, for each participant, we calculated an asymmetry index for the cortical VMA as:

$$Cortical\ VMA = \frac{(lower\ vertical\ surface\ area - upper\ vertical\ surface\ area)}{mean(lower\ vertical\ surface\ area, upper\ vertical\ surface\ area)} \times 100 \quad (2)$$

A cortical VMA index of 0 indicates no difference in surface area between the lower and upper vertical meridian. As the asymmetry between the lower and upper vertical meridian increases, so does the magnitude of the cortical VMA. A negative VMA index indicates an inverted VMA; more surface area for the upper than lower vertical meridian.

The magnitude of the cortical HVA was similar for children and adults, around 80 for both (p = 0.782, independent samples t-test, **Fig 7A**). However, the magnitude of the cortical VMA differed between children and adults (p = 0.001, d = 1.12, independent samples t-test, **Fig 7A**); children had a VMA close to 0, whereas for adults it was 71.

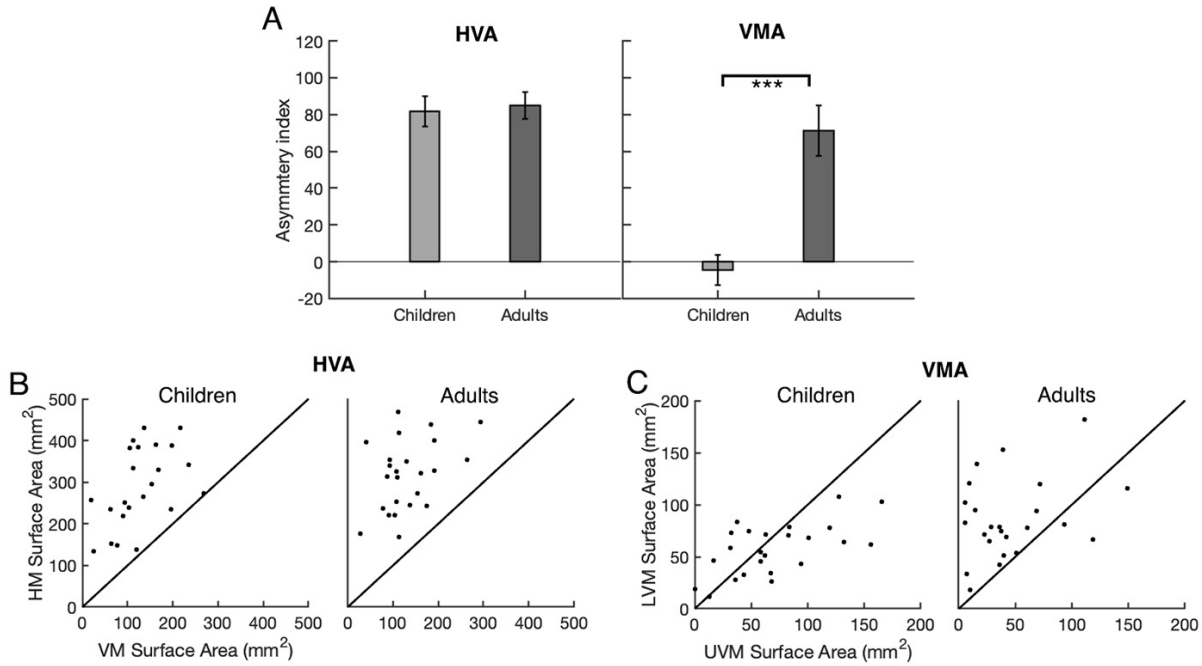

Fig. 7. Cortical HVA and VMA measurements from ±10° wedge-ROIs centered on the four polar angle meridians. (A) Magnitudes of the HVA and VMA asymmetry index for children and adults. Error bars indicate ±1 SEM. *** $p < 0.01$. **(B)** Scatterplots of the HVA for children and adults, with data above the diagonal reference line indicating more surface area the horizontal than vertical meridian. **(C)** Scatterplots of the VMA for children and adults, with data above the diagonal reference line indicating more surface area for the lower than upper vertical meridian, and vice versa.

The pattern of results for the cortical HVA was consistent across individual children and adults (**Fig. 7B**); every individual –24 of 24 children and 24 of 24 adults– showed greater surface area for the horizontal than vertical meridian. Similarly, the pattern of results for the cortical VMA was consistent across individual adults; most showed greater surface area for the lower than upper vertical meridian (**Fig. 7C**). For children, individual data were generally closer to the reference line than those of adults (**Fig. 7C**), but they varied; some had larger surface area for the lower than upper vertical meridian, but others had greater surface area for the upper than lower vertical meridian.

To ensure that our results were not dependent on arbitrary choices of vertex selection, we computed the HVA and VMA using two polar angle wedge sizes (±10 deg and ±20 deg) and six different eccentricity ranges (HVA: **Supplementary Figs. S4, S5;** VMA: **Supplementary Figs. S6, and S7)**. For all eccentricity ranges there was a robust HVA in adults and children, and the VMA was always greater in adults than children.

Finally, we assessed whether the lack of a cortical VMA in children could be an artifact of within-scan motion by correlating the magnitude of the asymmetry indices with participant motion. The magnitude of the cortical VMA did not correlate with participant motion, for adults (r = 0.05, p =

0.801) or children (r = -0.15, p = 0.459), indicating that the lack of cortical VMA in the children was not due to group differences in within-scan motion. Likewise, the magnitude of the cortical HVA did not correlate with participant motion for adults (r = 0.15, p = 0.484) or children (r = -0.13, p = 0.534).

DISCUSSION

We quantified and compared measurements of the cortical representation of the visual field between adults and children: visual field map surface area and cortical magnification. As expected, both the total surface area within each of the V1, V2, and V3 maps and cortical magnification as a function of eccentricity were similar between adults and children (Conner et al., 2004; Dekker et al., 2019). We then investigated a new domain of comparison: V1 surface area as a function of polar angle. First, these data revealed a new commonality between adults and children–both showed much greater V1 surface area representing the horizontal than the vertical meridian of the visual field. Second, these data revealed a striking difference–adults had greater V1 surface area representing the lower vertical than upper vertical meridian, whereas children did not. This pronounced difference in V1 suggests that primary sensory cortices continue to change beyond childhood. This late-stage change is surprising given that many properties of primary sensory and motor areas develop early (Bourne and Rosa, 2006; Dekker et al., 2019; Ellis et al., 2021; Flechsig, 1920; Gomez et al., 2018; Lebenberg et al., 2019).

The overall surface area of V1, V2, and V3 is stable between childhood and adulthood

There was a close match between adults and children in: map surface area, the degree of variability of map surface area, and total cortical surface area. This is consistent with reports showing that the surface areas of V1, V2, and V3 are similar between adults and children (Dekker et al., 2019) and that the total surface area of the cortical sheet is adult-like by age 10 (Bethlehem et al., 2022; Brown et al., 2012; Raznahan et al., 2011). Notably, the coefficients of variation reported for V1, V2, and V3 were similar to those reported from adult data from the HCP dataset, all around 0.2 (Benson et al., 2021b). A coefficient of variation of 0.2 predicts a 2-fold range in map surface area when comparing the largest to smallest maps in sample sizes comparable to ours (20-30 participants, assuming approximately normal distributions), just as we found. A 2-fold range in V1 surface area has also been identified in infants under 5 years (Ellis et al., 2021). The substantial variability observed in the V1 surface area of infants, children, and adults, is consistent with variability in other structures in the visual system. Cone density varies about 3-fold across individuals (Curcio et al., 1987) and there is substantial variation in the size of the LGN and optic tract (Andrews et al., 1997; Miyata et al., 2022). An intriguing possibility is that these structures co-vary, such that an individual with high cone density will also tend to have a large optic tract, LGN, and V1. Some older, post-mortem work (Andrews et al., 1997), as well as recent in vivo measurements (Miyata et al., 2022; Silva et al., 2021; Taskin et al., 2022) suggest that this might be the case.

Cortical magnification as a function of eccentricity is stable between childhood and adulthood

Cortical magnification as a function of eccentricity in V1, V2, and V3 was similar between adults and children, consistent with prior neuroimaging reports (Conner et al., 2004; Dekker et al., 2019). fMRI work shows that eccentricity-dependent properties of adult V1 also exist in infant and child V1: for infants as young as 5 months, the spatial frequency tuning of visual field maps decreases with increasing eccentricity (Ellis et al., 2021) and children as young as 5 years have adult-like pRF sizes that become larger with increasing eccentricity (Dekker et al., 2019; Gomez et al., 2018). It is likely that the eccentric representation of the visual field is specified prenatally and fine-tuned by visual experience early in life (Arcaro and Livingstone, 2017; Ellis et al., 2021; Huberman et al., 2008; Shatz, 1996).

Surprisingly, however, foveal cone density continues to increase into adolescence, as cells migrate and pack more densely towards the fovea (Hendrickson et al., 2012; Vajzovic et al., 2012). This could have some effect at the level of the cortex. There is a tendency in our cortical magnification data to see slightly greater magnification near the foveal representation of the visual field in adults than children. This suggests that adults might also have more foveal tissue than children, especially in V2 and V3. One possibility is that the effect is more apparent in V2 and V3, as these maps have greater cortical magnification of the fovea than V1 (Schira et al., 2009). Cortical mapping of the fovea is difficult (Dougherty et al., 2003; Himmelberg et al., 2021; Schira et al., 2009) and retinotopic methods focusing on precisely and accurately mapping the foveal confluence may find that the development of this region is matched to retinal development, which reaches maturity by around 15 years of age (Hendrickson et al., 2012; Vajzovic et al., 2012).

Cortical magnification as a function of polar angle changes between childhood and adulthood

We identified a cortical HVA in adults, and for the first time, in children. Both had roughly twice as much surface area representing the horizontal than vertical meridian of the visual field. These two groups are now the fifth and sixth to show greater V1 surface area representing the horizontal than vertical meridian (Benson et al., 2021a; Himmelberg et al., 2021, 2022a; Silva et al., 2018). This finding is consistent with the notion that targeted fMRI measurements made with high signal-to-noise are highly replicable across groups with typical sample sizes (20-30) (Himmelberg et al., 2021, 2022b).

In contrast, we identified a prominent dissimilarity in the cortical VMA between adults and children. Children had no difference in the amount of V1 surface area representing the lower and upper vertical meridians of the visual field. Conversely, adults had more V1 surface area representing the lower than upper vertical meridian, consistent with prior work (Benson et al., 2021a; Himmelberg et al., 2021, 2022a; Silva et al., 2018). These findings parallel recent psychophysical findings showing that children have an HVA but no VMA in visual performance (Carrasco et al., 2022), whereas adults have both (Abrams et al., 2012; Barbot et al., 2021;

Carrasco et al., 2001; Greenwood et al., 2017; Hanning et al., 2022; Himmelberg et al., 2020). Nonetheless, the fMRI data do not perfectly match the psychophysical data. For example, the magnitude of the behavioral HVA is smaller in children than in adults (Carrasco et al., 2022), whereas the cortical HVA is the same for both children and adults. There may be developmental changes outside V1 or changes in neural tuning –rather than surface area– that contribute to the larger behavioral HVA in adults. To better understand the link between cortical measures and visual performance at different locations in the visual field, we will measure both neural properties of V1 and visual performance and use these measurements to develop a computational model that explicitly links differences in the distribution of V1 properties to visual performance at different locations in the visual field.

Neural and behavioral evidence for developmental changes in the early human visual system

Because much of the early visual system, from the eye to V1, matures at a young age (Conner et al., 2004; Dekker et al., 2019; Ellis et al., 2021; Gomez et al., 2018), it is surprising to observe a large difference in the organization of V1 at a relatively late age (i.e., beyond the 6-12 years of age range tested here). Nonetheless, many features of the visual system continue to develop beyond adolescence.

The development of the human brain is protracted relative to non-human primates (Boothe et al., 1985; Kiorpes, 2016). Anatomical work shows that parts of the human visual system develop through childhood and mature well into adolescence. For example, optical coherence tomography (OCT) studies show that foveal and parafoveal retinal thickness, and parafoveal and perifoveal ganglion cell thickness, continue to thicken into adolescence (Bruce et al., 2013; Lee et al., 2015; Read et al., 2015), and foveal photoreceptors become elongated and migrate to become tightly packed around the fovea between childhood and adolescence (Hendrickson et al., 2012; Vajzovic et al., 2012). Thus, the retina continues to develop beyond childhood and these changes are likely to influence the response properties of downstream neurons such as circuits in visual cortex. Further, neuroimaging and post-mortem studies of human V1/V2 show that intracortical myelination rapidly increases through adolescence, and continues to increase into adulthood (Baum et al., 2022; Miller et al., 2012), indicating a relatively late maturation in cortical wiring of the human visual system. These phenomena are gradual and incremental, and do not imply the possibility of large-scale reorganization of the visual system in adulthood (Wandell and Smirnakis, 2009).

Consistent with the continued maturation of some parts of the visual system into adolescence, performance on basic visual tasks continues to improve well past childhood (Braddick and Atkinson, 2011). For example, contrast sensitivity matures around 12 years of age (Benedek et al., 2003, 2010; Gwiazda et al., 1997; Thibault et al., 2007), and both vernier acuity (Carkeet et al., 1997; Skoczenski and Norcia, 2002) and visual-spatial integration (Kovács et al., 1999) continue to improve until around 14 years of age. All three of these tasks are plausibly dependent on the quality of the V1 representation: V1 neurons are highly sensitive to contrast (Albrecht and

Hamilton, 1982; Boynton et al., 1999; Himmelberg and Wade, 2019; Marquardt et al., 2018; Vinke et al., 2022) and are likely to limit contrast sensitivity (Himmelberg et al., 2022a; Virsu and Rovamo, 1979); vernier acuity depends on the positional information encoded by V1 neurons (Fahle and Schmid, 1988; Stanley, 1991); and visual-spatial integration depends on local orientation information extracted and integrated by V1 neurons (Gilbert et al., 1996). The late maturation of visual performance on these tasks may reflect developmental changes in the response properties of V1 neurons or how V1 output is used by downstream neurons –or visual field maps– in the service of perception.

Biological underpinnings

The cortical VMA is a contrast between the cortical representation of the lower and upper portions of the vertical meridian of the visual field; in principle, the VMA could arise from an increase in the lower or a decrease in the upper vertical meridian representation. Our data suggest that the cortical VMA in adults reflects an increase in the surface area representing the lower vertical meridian of the visual field. We propose two possible neural underpinnings of this finding: changes in the spatial tuning of V1 receptive fields, or local changes in properties of V1 tissue along the lower vertical meridian.

The VMA might emerge in adults due to remapping of the receptive fields along the lower vertical meridian. From childhood to adulthood, the receptive fields of V1 neurons near the lower vertical meridian could migrate closer to the lower vertical meridian–just as photoreceptors migrate closer to the fovea (Hendrickson et al., 2012; Vajzovic et al., 2012). This would effectively increase receptive field coverage along the lower vertical meridian relative to the upper vertical meridian, resulting in a cortical VMA in adults. Prior work shows that pRFs remap across development in lateral visual field maps; from childhood to adulthood, lateral occipital (LO) and temporal occipital (TO) pRF coverage increases in fovea and periphery, respectively (Gomez et al., 2019), and these changes result in an increase in the spatial precision of the pRFs in these regions (Gomez et al., 2019). Similarly, pRF remapping has been reported in dorsal maps, where pRF coverage becomes increasingly dense in the periphery between childhood and adulthood. For example, pRF sizes in IPS1 are larger and more eccentric in adults than children (Duffield and Gomez, 2021). Further, and as noted above, there is evidence of cone migration through adolescence (Hendrickson et al., 2012; Vajzovic et al., 2012) and such changes in cone position could impact the receptive field properties of downstream visual neurons.

The amount of V1 surface representing the lower vertical meridian could also increase due to changes in other tissue properties, such as dendritic spine density, glial cell properties, myelination, and remodeling of the extracellular matrix. Neuroimaging studies have reported activation-dependent changes in tissue properties in adults undergoing skill learning and perceptual learning, suggesting that the structure of the human brain can show long-term plasticity in response to environmental demands. For example, work using diffusion tensor imaging (DTI) has provided evidence for microstructural changes in the hippocampus after a

spatial learning and memory task, likely due to reshaping of glial processes and the strengthening of dendritic spines (Sagi et al., 2012). Likewise, long-term training on a texture discrimination task is associated with an increase in fractional anisotropy along the inferior longtudinal fasciculus, connecting V1 to anterior regions of the brain (Kang et al., 2018). Similarly, fMRI work has shown that training in juggling is linked to transient increases in gray matter of motion-sensitive visual map hMT+ (Draganski et al., 2004), and faster phonetic learners have more white matter connections in parietal regions, indicating greater cortical myelination and thus more efficient processing (Golestani et al., 2002). Further, professional musicians have greater gray matter volume in motor, auditory, and visual regions than non-musicians (Gaser and Schlaug, 2003). None of these cases require the growth of new neurons, nor dramatic changes in neural tuning. Instead, these findings likely reflect changes in the microstructural properties in which neural circuits are embedded. A similar effect might explain our data. Although it is not yet known what task demands, if any, specifically require greater use of the lower vertical meridian in adults than in children, we hypothesize that a change in input or behavior could result in activation-dependent changes in V1 tissue properties at cortical regions encoding the lower vertical meridian, manifesting as a change in the amount of V1 surface area devoted to this region of the visual field.

Ecological considerations

Children showed adult-like measurements of V1 surface area representing the horizontal meridian of the visual field. The finding that the cortical and behavioral HVA emerge early in development parallels the finding that the HVA is found early in the visual pathways (e.g., the density of cone photoreceptors (Curcio et al., 1987, 1990)). Because of the importance of information along the horizon, many terrestrial animals have horizontal retinal streaks rather than circular fovea (Duke-Elder, 1958; Hughes, 1977; Wald, 1944); the human HVA may be a reflection of similar environmental factors. Given the possible ecological advantage of a perceptual HVA for both children and adults, it may be that the horizontal representation of the visual field in V1 is broadly specified in-utero and fine-tuned during early years of life, similar to how eccentricity representations are thought to be a part of an innate cortical blueprint in human and non-human primates (Arcaro and Livingstone, 2017; Ellis et al., 2021). However, the specific image properties that might be important along the horizontal meridian (and their relevance to behavior) are yet to be elucidated.

In contrast, children did not have a cortical VMA, matching their lack of a behavioral VMA. A possible ecological account of this phenomenon would propose that a lower visual field specialization emerges with age due to neural adaptation to regularities of the visual environment. As discussed in prior work (Carrasco et al., 2022), given children's height and behavior, a large portion of their perceptual world is within the upper portion of the visual field. Thus, a VMA would be detrimental to their interaction with their visual environment. As children grow to become adults and their height increases, their visual environment consists of more important events and actions below fixation–for example, visuomotor manipulation such as

reaching and tool use (Previc, 1990). This is congruent with evidence that the behavioral VMA emerges in late adolescence (Carrasco et al., 2022; Myers & Carrasco, 2020). We plan to investigate whether the cortical VMA emerges at a similar period by quantifying the cortical polar angle asymmetries in adolescents, allowing us to uncover whether the emergence of a cortical VMA is linked to the emergence of the behavioral VMA.

However, as mentioned above, it is not yet known what task demands, if any, specifically require greater use of the lower vertical meridian (rather than lower visual field) in adults than in children. Polar angle asymmetries in visual performance (Abrams et al., 2012; Barbot et al., 2021; Carrasco et al., 2001) and cortical surface area (Benson et al., 2021a; Himmelberg et al., 2021) are most pronounced at the cardinal meridians, gradually diminishing to the point that they are no longer present at intercardinal locations (Abrams et al., 2012; Barbot et al., 2021; Carrasco et al., 2001). Thus, any specialization must be primarily driven by the vertical meridian itself.

Conclusion

Many aspects of V1, V2, and V3 are mature by early childhood –map surface area, cortical magnification as a function of eccentricity, and greater surface area representing the horizontal than vertical meridian of the visual field. However, children, unlike adults, do not have a cortical asymmetry in the amount of V1 surface area representing the upper and lower vertical meridian. These findings reveal a late-stage change in the architecture of V1 that parallels the presence of a vertical meridian asymmetry in visual perception by adulthood.

METHODS

Participants

Raw retinotopy data were obtained from a previous fMRI study investigating receptive field development in children (Gomez et al., 2018). 24 children (ages 5-12 years old; 10 male, 14 female, mean = 8.8 years) and 24 adults (ages 22-27 years old, 13 male, 11 female, mean = 23.8 years) participated in the study. All participants had normal or corrected-to-normal vision. Written informed consent was obtained for all participants; all parents provided written consent for their child to participate in the study, and children provided written assent. The retinotopy experiment was conducted in accordance with the Declaration of Helsinki and was approved by the Institutional Review Board of Stanford University.

Retinotopic mapping experiment

For each adult, data were collected across two scan sessions (one anatomical and one functional session). For each child, data were collected over three sessions (one mock scanner training, one anatomical, and one functional session) across the span of a few months. First, to acclimatize children to the MRI scanner and to practice lying still, they were required to complete

training in a mock scanner. During the training, the child participant viewed a movie (~15 minutes) in the scanner and received live-feedback of head motion. Next, each participant completed an MRI session in which a full brain anatomical image was obtained. Finally, each participant completed an fMRI session in which they completed four runs of a retinotopic mapping experiment to measure population receptive field (pRF) parameters across visual cortex.

The pRF stimulus and the MRI and fMRI acquisition parameters were identical to prior work (Gomez et al., 2018). However, the data were reanalyzed, thus the MRI and fMRI preprocessing and the implementation of the pRF model, differ.

fMRI stimulus display

Participants viewed the pRF stimulus from within the scanner bore; the stimulus image was projected onto an acrylic screen using a rear-projection LCD projector (Eiki LC-WUL100L Projector). The projected image had a resolution of 1024x768. Participants viewed the screen from a distance of 265 cm inside the scanner bore using an angled mirror that was mounted on the head coil.

pRF stimulus

Retinotopic maps were measured using pRF modeling (Dumoulin and Wandell, 2008). The pRF stimulus was generated using MATLAB and was projected onto the fMRI stimulus display in the scanner bore using the Psychophysics Toolbox v3 (Kleiner et al., 2007). The pRF stimulus consisted of 100% contrast black and white checkerboard patterns that were presented within a bar aperture that swept across the screen for the duration of each scan, as in (Dumoulin and Wandell, 2008). The checkerboard pattern was windowed within a circular aperture that had a radius of 7°. The checkerboard pattern was revealed through a bar aperture (width = 3°, length = 14°) that swept across the screen. Each step was synchronized to the fMRI image acquisition (TR 2 s). There were 8 sweeps in total and each sweep began at the edge of the circular aperture. Horizontal and vertical sweeps covered the entire diameter of the circular aperture, whereas diagonal sweeps only traversed half the circular aperture, with the second half of the diagonal sweep being replaced with a blank gray screen. The full stimulus run lasted 3 mins 24 s. The stimulus image updated 2 times per second without intermediate blanks.

During each pRF stimulus run, participants were instructed to maintain fixation on a small spaceship (~0.5° in size) located in the center of the display that acted as a fixation stimulus throughout the entire scan. Participants performed a fixation task in which they were required to respond, via a button box, when the spaceship changed color.

Anatomical and functional data acquisition

Anatomical and functional data were acquired on a 3-Tesla GE Discovery MR750 scanner (GE Medical Systems) at the Center for Cognitive Neurobiological Imaging at Stanford University.

Quantitative magnetic resonance imaging (qMRI) full-brain anatomical measurements were obtained using the protocols in (Mezer et al., 2013) and with a phase-array 32-channel head coil. T1 relaxation times were measured from four spoiled gradient echo (spoiled-GE) images (flip angles: 4°, 10°, 20°, 40°; TR: 14 ms; TE: 2.4 ms; voxel size: 0.8 mm x 0.8 mm x 1.0mm). To correct field inhomogeneity, four additional spin inversion recovery (SEIR) images were collected (inversion times: 50, 400, 1200, 2400 ms; TR: 3 s; echo time set to minimum full and 2x acceleration; voxel size: 2 mm x 2 mm x 4mm) with an echo planar imaging (EPI) read-out, a slab inversion pulse, and spatial fat suppression.

Four functional EPI images were acquired for each participant using a 16-channel head coil and a multiband EPI sequence (TR, 2 s; TE, 30 ms; voxel size, 2.4mm^3 isotropic; multiband acceleration factor, 2, 28 slices) with slices aligned parallel to the parieto-occipital sulcus.

Processing of anatomical data

qMRI anatomical measurements (i.e., the spoiled GE image and the SEIR images) were processed using mrQ software (Mezer et al., 2013). The mrQ pipeline corrects for radiofrequency coil bias using the SERI images to produce accurate proton density and T1 fits across the brain. These fits were used to compute a T1w anatomical image for each participant.

Following this, *fMRIPrep* v.20.0.1 (Esteban et al., 2019; Gorgolewski et al., 2011) was used to process the anatomical and functional data. For each participant, the T1w anatomical image was corrected for intensity inhomogeneity and skull stripped. The anatomical image was then automatically segmented into cerebrospinal fluid, cortical white-matter, and cortical gray-matter using *fast* (Zhang et al., 2001). Cortical surfaces in the participant's native space (called *fsnative* in FreeSurfer) at the midgray, pial, and white matter depth were reconstructed using FreeSurfer's *recon-all* (Dale et al., 1999).

Processing of functional data

The following processing was performed on each participant's functional data. First, a reference volume (and skull stripped version) was generated using custom methodology of *fMRIprep*. An estimated distortion of the B0-non uniformity map was used to generate a corrected functional reference image; this reference image was co-registered to the anatomical image using six degrees of freedom. Following this, head-motion parameters with respect to the functional reference were estimated before any spatiotemporal filtering. Each functional image was then slice-time corrected. All slices were realigned to the middle of each TR. These slice-time

corrected data were then resampled to the T1w anatomical space via a one-shot interpolation consisting of all the pertinent transformations. These preprocessed time-series data were then resampled to the *fsnative* surface for each participant, by averaging across the cortical ribbon. For each participant, this processing was completed for each of the four functional scans.

Within-scan motion: calculating Framewise Displacement

Framewise displacement (FD) was calculated as a quality metric for motion artifacts based on the framewise differences of the 3D translation (mm) and rotation (radians) estimates of motion during the scan. First, we took the absolute framewise difference of the translation and rotation metrics across three dimensions:

$$\Delta d_{tx} = d_{(t-1)x} - d_{tx} \qquad (3)$$

Where d represents the translational motion estimate, t represents time, and x represents the slice dimension.

To combine the rotational motion with translational motion in mm units, we estimated the arc length displacement of the rotational motion metric from the origin by approximating the distance between the center of the head and the cerebral cortex with a radius of 50 mm (Power et al., 2012).

$$\Delta\alpha_t = 50 \,.\, (\pi/180) \,.\, (\alpha_{(t-1)} - \alpha_t) \qquad (4)$$

Where α represents the rotational motion estimate, and t represents time.

Finally, we calculated the FD as the sum of the framewise difference of the translational and rotational metrics across three dimensions:

$$FD_t = |\Delta d_{tx}| + |\Delta d_{ty}| + |\Delta d_{tz}| + |\Delta\alpha_t| + |\Delta\beta_t| + |\Delta\gamma_t| \qquad (5)$$

For each participant, we counted the number of times the FD exceeded the threshold of 0.5 mm across scanning sessions (see *fMRIprep* documentation for the set threshold (Esteban et al., 2019)).

Implementing the pRF model on the cortical surface to compute retinotopic maps

The pRF model was implemented using vistasoft (Vista Lab, Stanford University). We used customized code to run the pRF model on the cortical surface. Here, a pRF was modeled as a circular 2D Gaussin which is parameterized by values at each vertex for *x* and *y* (specifying the center position of the 2D Gaussian in the visual field) and *σ,* the standard deviation of the 2D-

Gaussian (specifying the size of the receptive field). This 2D Gaussian was multiplied (pointwise) by the stimulus contrast aperture and was then convolved with the hemodynamic response function (HRF) to predict the BOLD percent signal change (or BOLD signal). We parameterized the HRF using 5 values, describing a difference of two gamma functions (Dumoulin and Wandell, 2008; Friston et al., 1998; Harvey and Dumoulin, 2011; Himmelberg et al., 2021; Worsley et al., 2002).

For each participant, the time-series data were averaged across the four preprocessed functional images to create an average time-series. This average time-series was then transformed to a BOLD signal. For each participant, the pRF model was fit to the BOLD signal for each vertex on the *fsnative* surface (i.e. the native surface generated by Freesurfer). The pRF model finds the optimal pRF parameters for each vertex by minimizing the residual sum of squares between the predicted time-series and the BOLD signal. The pRF model was fit using a multi-stage coarse-to-fine approach (Harvey and Dumoulin, 2011). First, the data were temporally decimated by a factor of two to remove high frequency noise. Next, the pRF parameters (x, y, σ) were fit using a brute force grid search. The results were then taken as the starting point of a second-stage search fit. The estimated pRF parameters were then held fixed and the HRF parameters were fit by a search by choosing parameters that minimize the squared error between the data and the prediction averaged across vertices. Finally, the HRF parameters were held fixed and the pRF parameters were refit to the data in a final search fit. Only the vertices with a variance explained equal to or greater than 10% were included in all subsequent analyses.

Defining V1, V2, and V3

V1, V2, and V3 were defined as regions-of-interest (ROIs) by hand (M.M.H and E.T) using Neuropythy v0.11.9 (https://github.com/noahbenson/neuropythy; (Benson and Winawer, 2018)). Each ROI was defined on flatmaps of the cortical surface and extended from 0°-7° of eccentricity. The V1, V2, and V3 boundaries were defined as the center of the polar angle reversals that occurred at the vertical or horizontal meridians (Dumoulin and Wandell, 2008; Himmelberg et al., 2021; Wandell and Winawer, 2015).

Cortical magnification as a function of eccentricity

For each observer, we calculated the cortical magnification function (CMF) as a function of eccentricity for each of the V1, V2, and V3 ROIs using *Neuropythy* v0.11.9 (Benson and Winawer, 2018). For each participant, and for a given map, we calculated cortical magnification m(r), or mm^2 of cortex/$degrees^2$ of visual space, from 1° to 7° of eccentricity. We did so by finding the value Δr, given that 20% of the *fsnative* vertices had an eccentricity between $r - \Delta r$ *and* $r + \Delta r$. The surface area (mm^2) of these vertices was summed and divided by the amount of visual space (deg^2) encapsulated by the eccentricity ring, which is defined as $r \pm \Delta r$. The result of this is a measurement of an areal CMF from 1 through to 7° of eccentricity.

Cortical magnification as a function of polar angle

For each observer, we calculated localized measurements of V1 surface area (mm^2) representing the polar angle meridians. We did so by defining wedge-ROIs that were centered on the polar angle meridians in the visual field. These wedge-ROIs were defined using *Neuropythy* v0.11.9 and custom MATLAB code. The specific implementation of this analysis is described below and in prior work (Himmelberg et al., 2021, 2022a) and circumvents discontinuities in surface area that would arise if we had defined the wedge-ROIs using estimates of pRF centers alone (Benson and Winawer, 2018; Himmelberg et al., 2021).

In brief, the process was as follows. A wedge-ROI was centered on either the left or right horizontal meridian, the upper vertical meridian, or the lower vertical meridian. The polar angle width of the wedge-ROI varied, extending ±10°, ±20°, ±30°, ±40°, and ±50° in angle from the respective meridian. Each wedge-ROI extended from 1–7° of eccentricity. Unlike the 0°–7° limit we used for defining V1-V3, we excluded the central 1° from the wedge-ROI because polar angle representations can be noisy in the fovea (Dougherty et al., 2003; Himmelberg et al., 2021; Schira et al., 2009). Each wedge-ROI was used as a mask and was overlaid on a cortical surface area map. These maps specify the cortical surface area (in mm^2) of each vertex on the *fsaverage* surface. The amount of cortical surface representing the polar angle meridians was calculated by summing the surface area of the vertices that fell within the wedge-ROI mask.

Defining wedge-ROIs along the polar angle meridians

The following processes were completed for each observer using *Neuropythy* v0.11.9 (Benson and Winawer, 2018). First, the shortest distance on the *fsnative* surface between each pair of vertices and a polar angle meridian was calculated. The horizontal, upper, and lower vertical meridians in V1 were defined using manually defined line-ROIs that were drawn upon the polar angle pRF data. The vertical meridian line-ROI followed the trace of the defined V1 ROI. The line-ROIs were used to calculate three *cortical distance maps* per hemisphere; one for the upper vertical meridian, one for the lower vertical meridian, and one for the horizontal meridian. The cortical distance maps specified the distance (in mm) of each vertex from the meridian (i.e., there was one cortical distance map per meridian per participant). Thus, the vertices along the meridian itself had a distance value of 0 mm. This process was repeated for the left and right hemispheres of V1, so that the upper and lower vertical wedge-ROIs would span the left and right visual hemifield.

The V1 map was then divided into 8 log spaced eccentricity bands between 1° and 7° of eccentricity in the visual field. This ensured that the eccentricity bands were roughly equally spaced in V1. The eccentricity bands were used to calculate *sub-wedge-ROIs*. These would be later combined to form a *full wedge-ROI*. Thus, each wedge-ROI is formed of multiple smaller sub-wedge-ROIs that represent some eccentricity portion of the full wedge). The eccentricity bands were defined using retinotopic maps generated by Bayesian inference (Benson and

Winawer, 2018) to ensure that each eccentricity band was a continuous region of visual space. These Bayesian inference maps combine each participant's vertex-wise pRF estimates with a previously defined retinotopic template to denoise the estimate of the visual field. The polar angle maps were 'cleaned' using *Neuropythy* (Benson and Winawer, 2018), by implementing an optimization algorithm on the pRF polar angle fits in V1 for each participant. This minimization aims to adjust the pRF centers of the vertices as little as possible to simultaneously enforce a smooth cortical magnification map and correct the field-sign values across V1. Both the Bayesian inference eccentricity maps, and the cleaned polar angle maps, were only used for the wedge-ROI analysis.

For each wedge-ROI, and within each eccentricity band, we used the *cortical distance maps* to compute the distance of an iso-angle line that represented the outer boundary of the wedge-ROI in the visual field. We measured wedge-ROIs of multiple widths. The iso-angle line fell 10°, 20°, 30°, 40°, and 50° of angle away from a meridian. This effectively forms wedge-ROIs in the visual field that extend 10°, 20°, 30°, 40°, and 50° from a meridian. Our goal was to calculate the *distance* (in mm of cortex) of this iso-angle line from a meridian. To do so, we used the cleaned pRF polar angle data and the *cortical distance maps* to calculate the average distance of the vertices in a region of V1 that fell ±8° around the iso-angle line polar angle value. The average distance of these vertices represents the distance on the cortex (in mm) of the iso-angle line from a meridian. This process was repeated for each eccentricity band.

For each eccentricity band we identified the vertices with a cortical distance value of 0 mm (i.e., those along a meridian, and thus the center boundary of the wedge-ROI) and with a distance pertaining to each iso-angle boundary (i.e., 10° through to 50°). This was repeated for each eccentricity band to generate sub-wedge-ROIs. These sub-wedge-ROIs were combined to create a full wedge-ROI. This process was repeated for each meridian and each hemisphere. Together, these steps identify the vertices that will form the center-boundary of the wedge-ROI (i.e., a polar angle meridian) and the vertices that form the outer-boundary of that wedge-ROI. The vertices within these boundaries represent a continuous wedge in the visual field.

The final step was to use the full wedge-ROI as a mask on *cortical surface area maps*. These maps are generated for each observer and denote the surface area (in mm^2) of each vertex on the *fsnative* surface. The wedge-ROI was overlaid on the cortical surface area map and the surface area of the vertices within the wedge-ROI were summed to calculate the surface area of the wedge-ROI. This was repeated for each meridian, and each hemisphere. To calculate the amount of surface area dedicated to processing the horizontal meridian, the surface area of the left and right horizontal wedge-ROIs were summed together. To calculate the amount of surface area dedicated to processing the upper vertical meridian, the surface area of the wedge-ROIs extending from the left and right sides of the upper vertical meridian (thus right and left hemisphere's of V1, respectively) were summed together. Likewise, to calculate the surface area dedicated to processing the lower vertical meridian, the wedge-ROIs extending the left and right sides of the lower vertical meridian (again, right and left hemispheres of V1, respectively) were

summed together. The upper and lower vertical meridian wedge-ROIs were summed to calculate the surface area dedicated to processing the full vertical meridian.

Midgray, pial and white matter surfaces

Cortical surface area was measured using *cortical surface area maps* that were generated, using *FreeSurfer*, at three levels of surface depth; midgray, pial, and white matter. All main analyses were conducted on the midgray surface of the cortex which falls in the middle-depth of the cortical sheet between the pial and white matter surfaces. Supplemental analyses were calculated on pial (upper) and white matter (lower) surfaces. The cortical surface area of the vertices within the three maps differ; this is because the surface area of gyri at the pial surface and the sulci at the white matter surface tend to be large, whereas the sulci at the pial surface and gyri at the white matter surface tend to be small.

ACKNOWLEDGEMENTS

This work was funded by NIH grants RO1-EY027401 to M.C and J.W, P30-EY-013079 to Tony Movshon (PI), M.C, and J.W (module directors), RO1-EY022318 and RO1-EY023915 to K.G-S, and Princeton Neuroscience Institute start-up funds to J.G. We extend our thanks to Eline Kupers for her assistance in organizing and sharing the fMRI data from K.G-S's lab and Michael Barnett for assisting in data collection.

AUTHOR CONTRIBUTIONS

M.C and J.W conceived the experiments, J.G and K.G-S provided the data, M.M.H, E.T, J.G, and J.W analyzed the data, M.M.H, E.T, M.C, and J.W wrote the paper, and all authors edited the paper.

COMPETING INTEREST STATEMENT: The authors declare no competing financial interests.

REFERENCES

Abrams, J., Nizam, A., and Carrasco, M. (2012). Isoeccentric locations are not equivalent: the extent of the vertical meridian asymmetry. Vision Res. *52*, 70–78. https://doi.org/10.1016/j.visres.2011.10.016.

Albrecht, D.G., and Hamilton, D.B. (1982). Striate cortex of monkey and cat: contrast response function. J. Neurophysiol. *48*, 217–237. https://doi.org/0022-3077/82/0000-0000$01.25.

Andrews, T.J., Halpern, S.D., and Purves, D. (1997). Correlated size variations in human visual cortex, lateral geniculate nucleus, and optic tract. J. Neurosci. *17*, 2859–2868. https://doi.org/10.1523/JNEUROSCI.17-08-02859.1997.

Arcaro, M.J., and Livingstone, M.S. (2017). A hierarchical, retinotopic proto-organization of the primate visual system at birth. Elife *6*. https://doi.org/10.7554/eLife.26196.

Barbot, A., Xue, S., and Carrasco, M. (2021). Asymmetries in visual acuity around the visual field. J. Vis. *21*, 2. https://doi.org/10.1167/jov.21.1.2.

Baum, G.L., Flournoy, J.C., Glasser, M.F., Harms, M.P., Mair, P., Sanders, A.F.P., Barch, D.M., Buckner, R.L., Bookheimer, S., Dapretto, M., et al. (2022). Graded Variation In T1w/T2w Ratio During Adolescence: Measurement, Caveats, and Implications for Development of Cortical Myelin. J. Neurosci. https://doi.org/10.1523/JNEUROSCI.2380-21.2022.

Benedek, G., Benedek, K., Kéri, S., and Janáky, M. (2003). The scotopic low-frequency spatial contrast sensitivity develops in children between the ages of 5 and 14 years. Neurosci. Lett. *345*, 161–164. https://doi.org/10.1016/s0304-3940(03)00520-2.

Benedek, K., Janáky, M., Braunitzer, G., Rokszin, A., Kéri, S., and Benedek, G. (2010). Parallel development of contour integration and visual contrast sensitivity at low spatial frequencies. Neurosci. Lett. *472*, 175–178. https://doi.org/10.1016/j.neulet.2010.02.001.

Benson, N.C., and Winawer, J. (2018). Bayesian analysis of retinotopic maps. Elife *7*, 1–29. https://doi.org/10.7554/eLife.40224.

Benson, N.C., Kupers, E.R., Barbot, A., Carrasco, M., and Winawer, J. (2021a). Cortical magnification in human visual cortex parallels task performance around the visual field. Elife *10*. https://doi.org/10.7554/eLife.67685.

Benson, N.C., Yoon, J.M.D., Forenzo, D., Engel, S.A., Kay, K.N., and Winawer, J. (2021b). Variability of the surface area of the V1, V2, and V3 maps in a large sample of human observers. bioRxiv.

Bethlehem, R.A.I., Seidlitz, J., White, S.R., Vogel, J.W., Anderson, K.M., Adamson, C., Adler, S., Alexopoulos, G.S., Anagnostou, E., Areces-Gonzalez, A., et al. (2022). Brain charts for the human lifespan. Nature 1–11. https://doi.org/10.1038/s41586-022-04554-y.

Boothe, R.G., Dobson, V., and Teller, D.Y. (1985). Postnatal development of vision in human and nonhuman primates. Annu. Rev. Neurosci. *8*, 495–545. https://doi.org/10.1146/annurev.ne.08.030185.002431.

Bourne, J.A., and Rosa, M.G.P. (2006). Hierarchical development of the primate visual cortex, as revealed by neurofilament immunoreactivity: early maturation of the middle temporal area (MT). Cereb. Cortex *16*, 405–414. https://doi.org/10.1093/cercor/bhi119.

Boynton, G.M., Demb, J.B., Glover, G.H., and Heeger, D.J. (1999). Neuronal basis of contrast discrimination. Vision Res. *39*, 257–269. https://doi.org/10.1016/S0042-6989(98)00113-8.

Braddick, O., and Atkinson, J. (2011). Development of human visual function. Vision Res. *51*, 1588–1609. https://doi.org/10.1016/j.visres.2011.02.018.

Brown, T.T., Kuperman, J.M., Chung, Y., Erhart, M., McCabe, C., Hagler, D.J., Jr, Venkatraman, V.K., Akshoomoff, N., Amaral, D.G., Bloss, C.S., et al. (2012). Neuroanatomical assessment of biological maturity. Curr. Biol. *22*, 1693–1698. https://doi.org/10.1016/j.cub.2012.07.002.

Bruce, A., Pacey, I.E., Bradbury, J.A., Scally, A.J., and Barrett, B.T. (2013). Bilateral changes in foveal structure in individuals with amblyopia. Ophthalmology *120*, 395–403. https://doi.org/10.1016/j.ophtha.2012.07.088.

Carkeet, A., Levi, D.M., and Manny, R.E. (1997). Development of Vernier acuity in childhood. Optom. Vis. Sci. *74*, 741–750. https://doi.org/10.1097/00006324-199709000-00022.

Carrasco, M., Talgar, C.P., and Cameron, E.L. (2001). Characterizing visual performance fields: effects of transient covert attention, spatial frequency, eccentricity, task and set size. Spat. Vis. *15*, 61–75. https://doi.org/10.1163/15685680152692015.

Carrasco, M., Roberts, M., Myers, C., and Shukla, L. (2022). Visual field asymmetries vary between children and adults. Curr. Biol. *32*, R509–R510. https://doi.org/10.1016/j.cub.2022.04.052.

Conner, I.P., Sharma, S., Lemieux, S.K., and Mendola, J.D. (2004). Retinotopic organization in children measured with fMRI. J. Vis. *4*, 509–523. https://doi.org/10.1167/4.6.10.

Curcio, C.A., Sloan, K.R., Packer, O., Hendrickson, A.E., and Kalina, R.E. (1987). Distribution of cones in human and monkey retina: Individual variability and radial asymmetry. Science *236*, 579–582. https://doi.org/10.1126/science.3576186.

Curcio, C.A., Sloan, K.R., Kalina, R.E., and Hendrickson, A.E. (1990). Human photoreceptor topography. J. Comp. Neurol. *292*, 497–523. https://doi.org/10.1002/cne.902920402.

Dale, A.M., Fischl, B., and Sereno, M.I. (1999). Cortical surface-based analysis: I. Segmentation and surface reconstruction. Neuroimage https://doi.org/10.1006/nimg.1998.0395.

Daniel, P.M., and Whitteridge, D. (1961). The representation of the visual field on the cerebral cortex in monkeys. J. Physiol. *159*, 203–221. https://doi.org/10.1113/jphysiol.1961.sp006803.

Dekker, T.M., Schwarzkopf, D.S., de Haas, B., Nardini, M., and Sereno, M.I. (2019). Population receptive field tuning properties of visual cortex during childhood. Dev. Cogn. Neurosci. *37*, 100614. https://doi.org/10.1016/j.dcn.2019.01.001.

Dougherty, R.F., Koch, V.M., Brewer, A.A., Fischer, B., Modersitzki, J., and Wandell, B.A.

(2003). Visual field representations and locations of visual areas v1/2/3 in human visual cortex. J. Vis. *3*, 586–598. https://doi.org/10.1167/3.10.1.

Draganski, B., Gaser, C., Busch, V., Schuierer, G., Bogdahn, U., and May, A. (2004). Neuroplasticity: changes in grey matter induced by training. Nature *427*, 311–312. https://doi.org/10.1038/427311a.

Duffield, S., and Gomez, J. (2021). Dorsal stream receptive field development entails growing visual field coverage. J. Vis. *21*, 2413–2413. https://doi.org/10.1167/jov.21.9.2413.

Duke-Elder, S. (1958). System of Ophthalmology Vol. 1 The Eye in Evolution (Henry Kimpton).

Dumoulin, S.O., and Wandell, B.A. (2008). Population receptive field estimates in human visual cortex. Neuroimage *39*, 647–660. https://doi.org/10.1016/j.neuroimage.2007.09.034.

Ellis, C.T., Yates, T.S., Skalaban, L.J., Bejjanki, V.R., Arcaro, M.J., and Turk-Browne, N.B. (2021). Retinotopic organization of visual cortex in human infants. Neuron *109*, 2616–2626.e6. https://doi.org/10.1016/j.neuron.2021.06.004.

Esteban, O., Markiewicz, C.J., Blair, R.W., Moodie, C.A., Isik, A.I., Erramuzpe, A., Kent, J.D., Goncalves, M., DuPre, E., Snyder, M., et al. (2019). fMRIPrep: a robust preprocessing pipeline for functional MRI. Nat. Methods *16*, 111–116. https://doi.org/10.1038/s41592-018-0235-4.

Fahle, M., and Schmid, M. (1988). Naso-temporal asymmetry of visual perception and of the visual cortex. Vision Res. *28*, 293–300. https://doi.org/10.1016/0042-6989(88)90157-5.

Fassbender, C., Mukherjee, P., and Schweitzer, J.B. (2017). Reprint of: Minimizing noise in pediatric task-based functional MRI; Adolescents with developmental disabilities and typical development. Neuroimage *154*, 230–239. https://doi.org/10.1016/j.neuroimage.2017.05.007.

Flechsig, P.E. (1920). Anatomie des menschlichen Gehirns und Rückenmarks auf myelogenetischer Grundlage (G. Thieme).

Friston, K.J., Williams, S., Howard, R., Frackowiak, R.S.J., and Turner, R. (1996). Movement-Related effects in fMRI time-series. Magnetic Resonance in Medicine *35*, 346–355. https://doi.org/10.1002/mrm.1910350312.

Friston, K.J., Fletcher, P., Josephs, O., Holmes, A., Rugg, M.D., and Turner, R. (1998). Event-Related fMRI: Characterizing Differential Responses. Neuroimage *7*, 30–40. https://doi.org/10.1006/nimg.1997.0306.

Gaser, C., and Schlaug, G. (2003). Brain structures differ between musicians and non-musicians. J. Neurosci. *23*, 9240–9245. .

Gilbert, C.D., Das, A., Ito, M., Kapadia, M., and Westheimer, G. (1996). Spatial integration and cortical dynamics. Proc. Natl. Acad. Sci. U. S. A. *93*, 615–622. https://doi.org/10.1073/pnas.93.2.615.

Golestani, N., Paus, T., and Zatorre, R.J. (2002). Anatomical correlates of learning novel speech sounds. Neuron *35*, 997–1010. https://doi.org/10.1016/s0896-6273(02)00862-0.

Gomez, J., Natu, V., Jeska, B., Barnett, M., and Grill-Spector, K. (2018). Development

differentially sculpts receptive fields across early and high-level human visual cortex. Nat. Commun. *9*, 788. https://doi.org/10.1038/s41467-018-03166-3.

Gomez, J., Drain, A., Jeska, B., Natu, V.S., Barnett, M., and Grill-Spector, K. (2019). Development of population receptive fields in the lateral visual stream improves spatial coding amid stable structural-functional coupling. Neuroimage *188*, 59–69. https://doi.org/10.1016/j.neuroimage.2018.11.056.

Gorgolewski, K., Burns, C.D., Madison, C., Clark, D., Halchenko, Y.O., Waskom, M.L., and Ghosh, S.S. (2011). Nipype: A flexible, lightweight and extensible neuroimaging data processing framework in Python. Front. Neuroinform. *5*. https://doi.org/10.3389/fninf.2011.00013.

Greenwood, J.A., Szinte, M., Sayim, B., and Cavanagh, P. (2017). Variations in crowding, saccadic precision, and spatial localization reveal the shared topology of spatial vision. Proc. Natl. Acad. Sci. U. S. A. *114*, E3573–E3582. https://doi.org/10.1073/pnas.1615504114.

Gwiazda, J., Bauer, J., Thorn, F., and Held, R. (1997). Development of spatial contrast sensitivity from infancy to adulthood: psychophysical data. Optom. Vis. Sci. *74*, 785–789. https://doi.org/10.1097/00006324-199710000-00017.

Hanning, N.M., Himmelberg, M.M., and Carrasco, M. (2022). Presaccadic attention enhances contrast sensitivity, but not at the upper vertical meridian. iScience *25*, 103851. https://doi.org/10.1016/j.isci.2022.103851.

Harvey, B.M., and Dumoulin, S.O. (2011). The relationship between cortical magnification factor and population receptive field size in human visual cortex: constancies in cortical architecture. Journal of Neuroscience *31*, 13604–13612. https://doi.org/10.1523/JNEUROSCI.2572-11.2011.

Hendrickson, A., Possin, D., Vajzovic, L., and Toth, C.A. (2012). Histologic Development of the Human Fovea From Midgestation to Maturity. American Journal of Ophthalmology *154*, 767–778.e2. https://doi.org/10.1016/j.ajo.2012.05.007.

Himmelberg, M.M., and Wade, A.R. (2019). Eccentricity-dependent temporal contrast tuning in human visual cortex measured with fMRI. Neuroimage *184*, 462–474. https://doi.org/10.1016/j.neuroimage.2018.09.049.

Himmelberg, M.M., Winawer, J., and Carrasco, M. (2020). Stimulus-dependent contrast sensitivity asymmetries around the visual field. J. Vis. *20*, 18. https://doi.org/10.1167/jov.20.9.18.

Himmelberg, M.M., Kurzawski, J.W., Benson, N.C., Pelli, D.G., Carrasco, M., and Winawer, J. (2021). Cross-dataset reproducibility of human retinotopic maps. Neuroimage *244*, 118609. https://doi.org/10.1016/j.neuroimage.2021.118609.

Himmelberg, M.M., Winawer, J., and Carrasco, M. (2022a). Linking individual differences in human primary visual cortex to contrast sensitivity around the visual field. Nat. Commun. *13*, 3309. https://doi.org/10.1038/s41467-022-31041-9.

Himmelberg, M.M., Gardner, J., and Winawer, J. (2022b). What has vision science taught us

about functional MRI? PsyArXiv https://doi.org/10.31234/osf.io/76mez.

Holmes, G., and Lister, W.T. (1916). Disturbances of vision from cerebral lesions, with special reference to the cortical representation of the macula. Brain *39*, 34–73. https://doi.org/10.1093/brain/39.1-2.34.

Huberman, A.D., Feller, M.B., and Chapman, B. (2008). Mechanisms underlying development of visual maps and receptive fields. Annu. Rev. Neurosci. *31*, 479–509. https://doi.org/10.1146/annurev.neuro.31.060407.125533.

Hughes, A. (1977). The Topography of Vision in Mammals of Contrasting Life Style: Comparative Optics and Retinal Organisation. In The Visual System in Vertebrates, F. Crescitelli, C.A. Dvorak, D.J. Eder, A.M. Granda, D. Hamasaki, K. Holmberg, A. Hughes, N.A. Locket, W.N. McFarland, D.B. Meyer, et al., eds. (Berlin, Heidelberg: Springer Berlin Heidelberg), pp. 613–756.

Inouye, T. (1909). Die Sehstorungen bei Schussverletzungen der Kortikalen Sehsphare: Nach Beobachtungen an Verwundeten der letszten japanischen Kriege (Leipzig: Engelmann).

Kang, D.-W., Kim, D., Chang, L.-H., Kim, Y.-H., Takahashi, E., Cain, M.S., Watanabe, T., and Sasaki, Y. (2018). Structural and Functional Connectivity Changes Beyond Visual Cortex in a Later Phase of Visual Perceptual Learning. Sci. Rep. *8*, 5186. https://doi.org/10.1038/s41598-018-23487-z.

Kiorpes, L. (2016). The Puzzle of Visual Development: Behavior and Neural Limits. J. Neurosci. *36*, 11384–11393. https://doi.org/10.1523/JNEUROSCI.2937-16.2016.

Kleiner, Brainard, Pelli, Broussard, Wolf, and Niehorster (2007). What's new in Psychtoolbox-3? Perception *36*, 1–16. .

Kovács, I. (2000). Human development of perceptual organization. Vision Res. *40*, 1301–1310. https://doi.org/10.1016/s0042-6989(00)00055-9.

Kovács, I., Kozma, P., Fehér, A., and Benedek, G. (1999). Late maturation of visual spatial integration in humans. Proc. Natl. Acad. Sci. U. S. A. *96*, 12204–12209. https://doi.org/10.1073/pnas.96.21.12204.

Lebenberg, J., Mangin, J.-F., Thirion, B., Poupon, C., Hertz-Pannier, L., Leroy, F., Adibpour, P., Dehaene-Lambertz, G., and Dubois, J. (2019). Mapping the asynchrony of cortical maturation in the infant brain: A MRI multi-parametric clustering approach. Neuroimage *185*, 641–653. https://doi.org/10.1016/j.neuroimage.2018.07.022.

Lee, H., Purohit, R., Patel, A., Papageorgiou, E., Sheth, V., Maconachie, G., Pilat, A., McLean, R.J., Proudlock, F.A., and Gottlob, I. (2015). In Vivo Foveal Development Using Optical Coherence Tomography. Invest. Ophthalmol. Vis. Sci. *56*, 4537–4545. https://doi.org/10.1167/iovs.15-16542.

Marquardt, I., Schneider, M., Gulban, O.F., Ivanov, D., and Uludağ, K. (2018). Cortical depth profiles of luminance contrast responses in human V1 and V2 using 7 T fMRI. Hum. Brain Mapp. *39*, 2812–2827. https://doi.org/10.1002/hbm.24042.

Mezer, A., Yeatman, J.D., Stikov, N., Kay, K.N., Cho, N.-J., Dougherty, R.F., Perry, M.L., Parvizi, J., Hua, L.H., Butts-Pauly, K., et al. (2013). Quantifying the local tissue volume and composition in individual brains with magnetic resonance imaging. Nat. Med. *19*, 1667–1672. https://doi.org/10.1038/nm.3390.

Miller, D.J., Duka, T., Stimpson, C.D., Schapiro, S.J., Baze, W.B., McArthur, M.J., Fobbs, A.J., Sousa, A.M.M., Sestan, N., Wildman, D.E., et al. (2012). Prolonged myelination in human neocortical evolution. Proc. Natl. Acad. Sci. U. S. A. *109*, 16480–16485. https://doi.org/10.1073/pnas.1117943109.

Miyata, T., Benson, N.C., Winawer, J., and Takemura, H. (2022). Structural covariance and heritability of the optic tract and primary visual cortex in living human brains.

Myers, C., and Carrasco, M. (2020). Adolescents' and adults' sensitivity differs around the visual field. J. Vis. *20*, 873–873. https://doi.org/10.1167/jov.20.11.873.

Poldrack, R.A., Paré-Blagoev, E.J., and Grant, P.E. (2002). Pediatric functional magnetic resonance imaging: progress and challenges. Top. Magn. Reson. Imaging *13*, 61–70. https://doi.org/10.1097/00002142-200202000-00005.

Power, J.D., Barnes, K.A., Snyder, A.Z., Schlaggar, B.L., and Petersen, S.E. (2012). Spurious but systematic correlations in functional connectivity MRI networks arise from subject motion. Neuroimage *59*, 2142–2154. https://doi.org/10.1016/j.neuroimage.2011.10.018.

Previc, F.H. (1990). Functional specialization in the lower and upper visual fields in humans: Its ecological origins and neurophysiological implications. Behav. Brain Sci. *13*, 519–542. https://doi.org/10.1017/S0140525X00080018.

Raznahan, A., Shaw, P., Lalonde, F., Stockman, M., Wallace, G.L., Greenstein, D., Clasen, L., Gogtay, N., and Giedd, J.N. (2011). How does your cortex grow? J. Neurosci. *31*, 7174–7177. https://doi.org/10.1523/JNEUROSCI.0054-11.2011.

Read, S.A., Collins, M.J., Vincent, S.J., and Alonso-Caneiro, D. (2015). Macular retinal layer thickness in childhood. Retina *35*, 1223–1233. https://doi.org/10.1097/IAE.0000000000000464.

Sagi, Y., Tavor, I., Hofstetter, S., Tzur-Moryosef, S., Blumenfeld-Katzir, T., and Assaf, Y. (2012). Learning in the fast lane: new insights into neuroplasticity. Neuron *73*, 1195–1203. https://doi.org/10.1016/j.neuron.2012.01.025.

Schira, M.M., Tyler, C.W., Breakspear, M., and Spehar, B. (2009). The foveal confluence in human visual cortex. Journal of Neuroscience *29*, 9050–9058. https://doi.org/10.1523/JNEUROSCI.1760-09.2009.

Shatz, C.J. (1996). Emergence of order in visual system development. Proc. Natl. Acad. Sci. U. S. A. *93*, 602–608. https://doi.org/10.1073/pnas.93.2.602.

Silva, M.F., Brascamp, J.W., Ferreira, S., Castelo-Branco, M., Dumoulin, S.O., and Harvey, B.M. (2018). Radial asymmetries in population receptive field size and cortical magnification factor in early visual cortex. Neuroimage *167*, 41–52. https://doi.org/10.1016/j.neuroimage.2017.11.021.

Silva, M.F., Harvey, B.M., Jorge, L., Canário, N., Machado, F., Soares, M., d'Almeida, O.C., and Castelo-Branco, M. (2021). Simultaneous changes in visual acuity, cortical population receptive field size, visual field map size, and retinal thickness in healthy human aging. Brain Struct. Funct. https://doi.org/10.1007/s00429-021-02338-0.

Sireteanu, R. (2000). Texture segmentation,"pop-out," and feature binding in infants and children. In Progress in Infancy Research, (Psychology Press), pp. 207–274.

Skoczenski, A.M., and Norcia, A.M. (2002). Late maturation of visual hyperacuity. Psychol. Sci. *13*, 537–541. https://doi.org/10.1111/1467-9280.00494.

Stanley, O.H. (1991). Cortical development and visual function. Eye *5 (Pt 1)*, 27–30. https://doi.org/10.1038/eye.1991.5.

Taskin, H.O., Qiao, Y., Sydnor, V.J., Cieslak, M., Haggerty, E.B., Satterthwaite, T.D., Morgan, J.I.W., Shi, Y., and Aguirre, G.K. (2022). Retinal ganglion cell endowment is correlated with optic tract fiber cross section, not density.

Thibault, D., Brosseau-Lachaine, O., Faubert, J., and Vital-Durand, F. (2007). Maturation of the sensitivity for luminance and contrast modulated patterns during development of normal and pathological human children. Vision Res. *47*, 1561–1569. https://doi.org/10.1016/j.visres.2007.03.009.

Vajzovic, L., Hendrickson, A.E., O'Connell, R.V., Clark, L.A., Tran-Viet, D., Possin, D., Chiu, S.J., Farsiu, S., and Toth, C.A. (2012). Maturation of the human fovea: correlation of spectral-domain optical coherence tomography findings with histology. Am. J. Ophthalmol. *154*, 779–789.e2. https://doi.org/10.1016/j.ajo.2012.05.004.

Vinke, L.N., Bloem, I.M., and Ling, S. (2022). Saturating Nonlinearities of Contrast Response in Human Visual Cortex. J. Neurosci. *42*, 1292–1302. https://doi.org/10.1523/JNEUROSCI.0106-21.2021.

Virsu, V., and Rovamo, J. (1979). Visual resolution, contrast sensitivity, and the cortical magnification factor. Exp. Brain Res. *37*, 475–494. https://doi.org/10.1007/BF00236818.

Wald, G. (1944). The vertebrate eye and its adaptive radiation. Gordon L. walls. Physiol. Zool. *17*, 348–350. https://doi.org/10.1086/physzool.17.3.30151843.

Wandell, B.A., and Smirnakis, S.M. (2009). Plasticity and stability of visual field maps in adult primary visual cortex. Nat. Rev. Neurosci. *10*, 873–884. https://doi.org/10.1038/nrn2741.

Wandell, B.A., and Winawer, J. (2015). Computational neuroimaging and population receptive fields. Trends Cogn. Sci. *19*, 349–357. https://doi.org/10.1016/j.tics.2015.03.009.

Wilke, M. (2014). Isolated assessment of translation or rotation severely underestimates the effects of subject motion in fMRI data. PLoS One *9*, e106498. https://doi.org/10.1371/journal.pone.0106498.

Worsley, K.J., Liao, C.H., Aston, J., Petre, V., Duncan, G.H., Morales, F., and Evans, A.C. (2002). A general statistical analysis for fMRI data. Neuroimage *15*, 1–15. https://doi.org/10.1006/nimg.2001.0933.

Zhang, Y., Brady, M., and Smith, S. (2001). Segmentation of brain MR images through a hidden Markov random field model and the expectation-maximization algorithm. IEEE Trans. Med. Imaging *20*, 45–57. https://doi.org/10.1109/42.906424.